ADVANCED MATERIALS INTERFACES
Open Access
www.advmatinterfaces.de

Triphasic Inter-Dimensional WS_2/Magnetic Lithium Iron Oxide Nanocomposite for Electromagnetic Interference Shielding

Sagnik Ghosh, Mustafa Mahmoud Aboulsaad, Sawssen Slimani, Johan Cedervall, Bagher Aslibeiki, Tomas Edvinsson, Gianni Barucca, Luca Vattuone, Davide Peddis, and Tapati Sarkar**

The widespread use of wireless devices and telecommunication networks has given rise to electromagnetic interference (EMI) pollution that can cause data corruption, critical device failure, and detrimental effects on wildlife and human health. Developing EMI shielding materials can block these harmful electromagnetic waves. This study explores inter-dimensional composite systems composed of dielectric and magnetic phases (WS_2/biphasic lithium iron oxide) for EMI shielding applications. WS_2 is a 2D material with unique dielectric properties and flake-like morphology that enhances surface effects. In contrast, biphasic magnetic lithium iron oxide nanocomposites have grain-like morphology with greater magnetic losses. The formation of interfaces between these two phases with different morphologies and dimensionalities leads to enhanced interfacial polarization loss. This work demonstrates that by carefully controlling the weight percentage of the two phases, and thereby the interfaces, the EMI shielding properties can be significantly enhanced. An optimum phase composition is determined that exhibits maximum shielding efficiency (SE_T ≈55.6 dB at 12.4 GHz) with high absorption shielding (SE_A ≈48.8 dB at 12.4 GHz), and an absorption coefficient more than 100% higher than either end member. The studied nanocomposites, with their tunable absorption and reflection capabilities, are suitable for a wide range of EMI shielding applications.

1. Introduction

The emergence of high-speed internet networks, such as 5G and 6G, has invoked a worldwide transformation in the wireless communication industry. Wireless communication devices like smartphones, smartwatches, laptops, desktops, and Wi-Fi routers have become an indispensable part of our daily life. These devices emit electromagnetic (EM) waves within the microwave frequency range (≈GHz). These EM waves can interfere with the functioning of other devices leading to catastrophic device failure, data corruption, and data packet loss. This kind of electromagnetic interference (EMI) poses a serious threat to sensitive equipment in healthcare and aviation security.[1–5] The adverse effects of EMI are not only confined to devices and electronic systems but are also evident on the health of humans and wildlife.[5,6] To address these concerns, researchers have focused on developing high-performance

S. Ghosh, M. M. Aboulsaad, B. Aslibeiki, T. Edvinsson, T. Sarkar
Department of Materials Science and Engineering
Uppsala University
Box 35, Uppsala SE-75103, Sweden
E-mail: sagnik.ghosh@angstrom.uu.se; tapati.sarkar@angstrom.uu.se

S. Slimani, D. Peddis
Department of Chemistry and Industrial Chemistry & Genova INSTM RU
nM2-Lab
University of Genova
Genova 16146, Italy

The ORCID identification number(s) for the author(s) of this article can be found under https://doi.org/10.1002/admi.202500687

DOI: 10.1002/admi.202500687

S. Slimani, D. Peddis
National Research Council, Institute of Structure of Matter, nM2-Lab
Via Salaria km 29.300, Monterotondo Scalo, Roma 00015, Italy

J. Cedervall
Department of Chemistry-Ångström Laboratory
Inorganic Chemistry
Box 538, Uppsala SE-751 21, Sweden

B. Aslibeiki
Faculty of Physics
University of Tabriz
Tabriz, Iran

G. Barucca
Department of Science and Engineering of Matter
Environment and Urban Planning
University Politecnica delle Marche
Via Brecce Bianche 12, Ancona 60131, Italy

L. Vattuone
Department of Physics
University of Genoa
Via Dodecaneso 33, Genoa 16146, Italy

EMI shielding materials. A good shielding material should block by reflection and/or absorption the incoming EM waves from reaching the victim device. Reflection occurs due to impedance mismatch at the air-material interface, while absorption requires the conversion of EM energy into heat through dielectric or magnetic loss mechanisms.[7] In this context, materials with high conductivity, large surface area, and good chemical and thermal stability are preferred for developing EMI shielding materials.

2D materials satisfy many of these criteria: they have large specific surface area, excellent dielectric properties, suitable morphologies, and vacancy defects.[8,9] Defects and polarized interfaces can generate polarization loss mechanisms resulting in absorption of EM waves.[10] Therefore, they have been increasingly used in developing efficient EMI shielding materials. Fan et al. investigated the shielding performance of lightweight MXene ($Ti_3C_2T_x$)/graphene hybrid foams in the X-band (8.2–12.4 GHz). High shielding effectiveness of 50.7 dB was obtained for the sample with 1:2 ratio of MXene and reduced graphene oxide (rGO). The improved shielding performance of the composite was attributed to its porous structure and high electrical conductivity.[11] 2D materials/ferrite-based composites have also been used to increase absorption and minimize shielding due to reflection. Absorption is affected by dielectric and magnetic losses while reflection is governed by impedance mismatch. In this context, the addition of magnetic nanoparticles like ferrites into the 2D-material systems creates a magneto-dielectric synergy. The dielectric and magnetic behavior of the composite is modified, which may reduce impedance mismatch. Moreover, since the ferrite and the 2D-material have very different dielectric properties, the formation of interfaces between them opens up the possibility of interfacial polarization loss and thus, better absorption of EM waves. Prasad et al. synthesized MoS_2-rGO/$CoFe_2O_4$ nanocomposites, which registered a maximum shielding effectiveness of ≈19.26 dB with shielding due to absorption (SE_A) accounting for ≈12.62 dB. The SE_A value of the triphasic composite was higher than those of the individual phases (MoS_2, rGO, $CoFe_2O_4$) as well as biphasic MoS_2-rGO.[12] MoS_2-rGO/Fe_3O_4 also exhibited a total shielding effectiveness of ≈8.27 dB, which was higher than that of the MoS_2-rGO composite.[13] Shen et al. modified the 2D-material/magnetic nanoparticle system further by introducing high-performance polymer. The resulting polyetherimide (PEI)/graphene@Fe_3O_4 (G@Fe_3O_4) composite foams registered a shielding effectiveness of 14.3–18.2 dB in the X-band. Moreover, the SE_A improved from 12.7 to 17.3 dB when the G@Fe_3O_4 loading was increased from 7 to 10 wt.%.[14]

The above reports are indicative of the advantages of magneto-dielectric synergy on EMI shielding properties of multiphasic composites, although the influence of the weight fractions of the magnetic and dielectric components on the shielding mechanism is less understood. Among the different types of 2D materials, transition metal dichalcogenides (TMDCs) are an emerging class with potential for a variety of applications. TMDCs have the empirical notation MX_2, where M = transition metal atom (W, Mo, Ti, etc.) and X = chalcogens like S, Te, and Se.[15] The layered structure, defects, and active surface sites typical of TMDCs offer great opportunities for polarization effects. They have been used in gas sensing devices,[16] as anodes in batteries,[17] and as charge-trapping layers in resistive switching devices and in optoelectronic synapses.[18] Recently, they have also garnered attention as EMI shielding materials. Apart from the most commonly studied MoS_2, tungsten disulfide (WS_2) is another important member of the TMDC family with potential for EMI shielding applications. Zhang et al. prepared WS_2–rGO architecture and obtained a total shielding effectiveness (SE_T) of 32 dB (frequency range: 2–18 GHz) for the composite with 5 wt.% rGO. The ratio of WS_2 and rGO affected the shielding parameters with dielectric loss mechanisms playing a major role in absorbing the incident EM waves.[19] Microwave absorption capability of WS_2 nanosheets in the 2–18 GHz range has been studied. WS_2 nanosheets produced by hydrothermal synthesis were loaded with wax. The highest reflection loss (RL) of −15.6 dB was attained by the wax sample containing 40 wt.% WS_2 and a thickness of 5.5 mm.[20] The good performance of these WS_2-based shielding materials indicates that WS_2 is suitable as a dielectric component in a multiphasic EMI shielding material. However, the possibility of magneto-dielectric synergy in WS_2-based hybrid systems remains less explored.

The preferred magnetic components for shielding applications are soft spinel ferrites, which are ferrimagnetic nanoparticles with low coercivity, high saturation magnetization, and high Curie temperature. Biphasic lithium iron oxide (54 wt.% α-$LiFe_5O_8$ / 46 wt.% α-$LiFeO_2$) has been reported to possess a mixture of ferrimagnetic (α-$LiFe_5O_8$) and paramagnetic (α-$LiFeO_2$) phases resulting in improved absorption due to formation of interfaces. The composite also retains a saturation magnetization of ≈36 emu g^{-1} and low coercivity (<50 Oe).[1] Considering their advantages, complementary properties, and contrasting morphologies, we investigate here the EMI shielding performance of WS_2/biphasic lithium iron oxide nanocomposites. Combining a biphasic ferrite with layered WS_2 gives us the possibility of exploring the behavior of a triphasic composite system.

2. Results and Discussion

X-ray diffraction patterns of the composites are shown in **Figure 1** and the corresponding weight fractions (wt.%) of the constituent phases are tabulated in Table 3. The lithium ferrite sample (L(100)) exhibits a superposition of α-$LiFe_5O_8$ cubic spinel phase ($P4_332$ space group) and rock salt α-$LiFeO_2$ phase ($Fd\bar{3}m$ space group). Based on previously reported work, the L(100) sample is composed of 54 wt.% α-$LiFe_5O_8$ and 46 wt.% α-$LiFeO_2$.[1] The XRD pattern of the WS_2 (W(100)) sample matches with the space group $P6_3mmc$. The characteristic reflections at 14.2°, 32.1°, 35.4°, and 43.4° correspond to the (002), (100), (102), and (006) crystallographic planes of WS_2. In addition, the reflection ≈56.9° has been attributed to the (110) plane of WS_2. Many of the reflections are broad and weak indicating low dimensionality of the WS_2 nanoflakes.[21–23] For the nanocomposites, the XRD patterns reveal a superposition of reflections corresponding to all three constituent phases (α-$LiFe_5O_8$, α-$LiFeO_2$, and WS_2). Additionally, a minor reflection appears at 2θ ≈23°, which can be attributed to a WO_3 impurity phase.[24] This impurity phase likely originated from oxidation of WS_2 during synthesis inside the autoclave, and under high temperature conditions.[25]

L. Vattuone
IMEM-CNR Genoa Unit
Via Dodecaneso 33, Genoa 16146, Italy

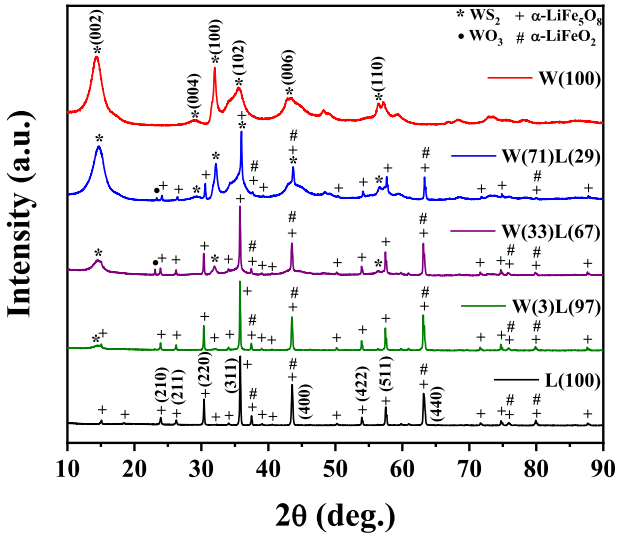

Figure 1. X-ray diffraction patterns of the nanocomposites ($\lambda = 1.5406$ Å).

The Raman spectrum of a representative sample, W(33)L(67) (**Figure 2**), shows three distinct Raman signatures obtained from different parts of the sample. These correspond to the spectra of α-$LiFe_5O_8$, WS_2, and WO_3, confirming the formation of the multiphasic composite. The two Raman peaks at ≈351 and ≈416 cm^{-1} correspond to the E^1_{2g} and A_{1g} modes of WS_2,[26,27] certifying the presence of WS_2 phase without any apparent peak broadening from amorphicity. The presence of WO_3 impurity phase is indicated by the peak ≈807 cm^{-1}.[28] The characteristic peaks of the α-$LiFe_5O_8$ phase are also visible in Figure 2.[1] However, peaks related to the α-$LiFeO_2$ phase are not seen clearly in any of the Raman signatures. The Raman spectrum of α-$LiFeO_2$ is characterized by three broad peaks located ≈180, 394, and 624 cm^{-1}.[1] These broad peaks must be overlapped by the background that is observed in the signal from the WS_2/WO_3/α-$LiFe_5O_8$

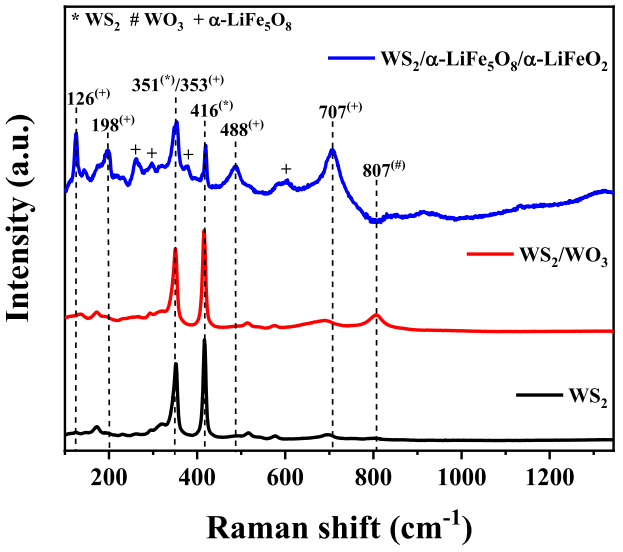

Figure 2. Raman spectra obtained from different parts of the W(33)L(67) composite under 532 nm laser illumination.

sample (Figure 2). Further details on the Raman spectra of biphasic lithium iron oxide can be found in our previous article.[1]

The normalized XPS survey spectra for W(100), L(100), and W(33)L(67) are shown in Figure S1 (Supporting Information). The main photoemission lines are marked in the figure. The energy scale was calibrated by setting the C 1s line at 284.5 eV (adventitious carbon). We observe that the W(100) sample also exhibits a non-negligible O 1s intensity, suggesting the presence of traces of tungstate. This conclusion is supported by the high-resolution W 4f and S 2p lines shown in **Figure 3**. The spectrum for W(100) shows not only the W 4f doublet expected for WS_2 (with peaks at 32.1 and 34.2 eV) but also a lower intensity doublet at higher binding energy (BE) (blue components at 35.9 and 38 eV). The BE of this doublet are close to those reported for tungstate and are assigned to oxidized W.[29] Moreover, an additional lower intensity doublet at 32.9 and 35.1 eV close to the main one (also green) is also needed to properly fit the asymmetric spectra. We tentatively assign it to WS_2 in a slightly different local environment. The presence of two doublets for WS_2 correlates with the presence of two S 2p doublets shown in Figure 3 (right panel). The more intense one with S $2p^{3/2}$ peak at 161.6 eV corresponds to regular WS_2 and the lower intensity one with a S $2p^{3/2}$ peak at 163.1 eV to the minority component. The higher BE for both W 4f and S 2p of this minority component suggests that they correspond to WS_2 close to tungstate patches. This assignment is supported by inspection of the spectra for W(33)L(67). For this sample, the intensity of the tungstate doublet (35.9 and 38 eV) as for W(100), is significantly larger than for W(100). Due to the higher amount of oxygen present, the relative intensity of the high-energy S 2p doublet with respect to the main line has also increased. The energy of the differently coordinated W atoms (doublet at 33.2 and 35.3 eV) is only slightly blue-shifted. There is a tiny contribution due to the W 5p line overlap with the tungstate peaks (see Figure 3), but their relatively low intensity does not affect our conclusions.

Inspection of **Figure 4** shows the effect of mixing between W(100) and L(100) for the Fe 3p and Li 1s lines. The Li 1s line at 57.4 eV is actually quite close to the Fe 3p line at 55.3 eV. Indeed, for the W(33)Li(67) composite, the centroid of the photoemission feature is at a higher BE since for this sample the Fe content is lower compared to L(100). For the L(100) sample, the main Li 1s peak has a BE (57.4 eV) close to the one reported for $LiFeO_2$.[30] We did not attempt to fit the Fe 3p lines including all multiplets due to their overwhelming complexity; instead, we fitted the Fe 2p line with two doublets and satellites as done in.[31] These authors, following also,[32] deconvoluted the spectra of the Fe 2p line into two peaks, corresponding to Fe^{2+} (709.18 and 722.65 eV) and Fe^{3+} (710.57 and 724.31 eV). Two satellite peaks were observed at 718.26 and 732.22 eV due to the Fe^{3+} oxidation state. In our experiment, we find for L(100), the main lines at 710.7 and 713.1 eV for the Fe $2p^{3/2}$ line. The former value is intermediate between those reported for $LiFe_5O_8$ and for $LiFeO_2$ while the latter one is higher than found reported previously for Fe^{3+}. The peaks with 13.5 higher BE are the corresponding Fe 2p ½ lines while the peaks at 719 and 733 eV are satellites. The corresponding Fe 2p line for the W(33)L(67) sample is quite similar indicating that the Fe atoms are not significantly affected by mixing with WS_2.

The room temperature M-H curves of the samples are presented in **Figure 5**. The W(100) sample (i.e., pure WS_2

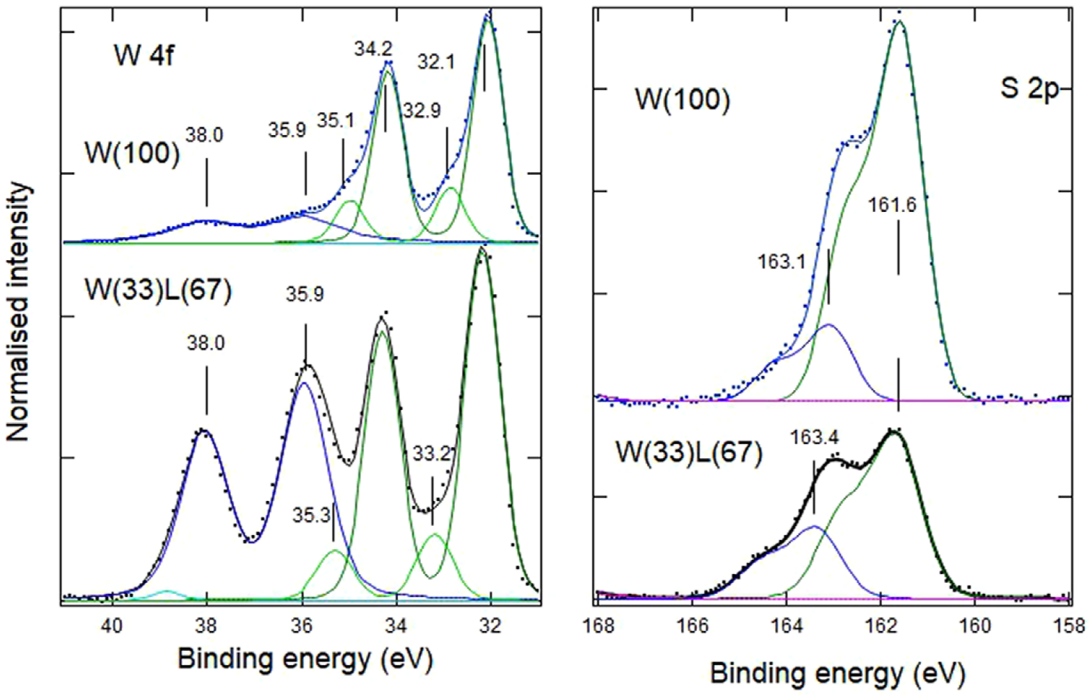

Figure 3. High resolution XPS spectra for W(100) and W(33)L(67) samples: W 4f (left) and S 2p (right).

nanoflakes) exhibits a diamagnetic behavior.[27] All the other samples exhibit mainly superparamagnetic behavior, and a clear monotonic increase in saturation magnetization is observed with increasing lithium iron oxide content in the nanocomposite system (**Table 1**). This enhancement in magnetic response is attributed to the presence of ferrimagnetic α-$LiFe_5O_8$ within the biphasic lithium iron oxide.

2.1. Internal Morphology and Interfaces in the Nanocomposites

The phases in the nanocomposites are morphologically distinct. This is seen in the SEM images in **Figure 6**a,b, where the two end members, L(100) and W(100), are shown. The biphasic lithium iron oxide shows granular morphology with irregular-shaped grains (<1 μm), Figure 6a. In contrast, Figure 6b depicts the

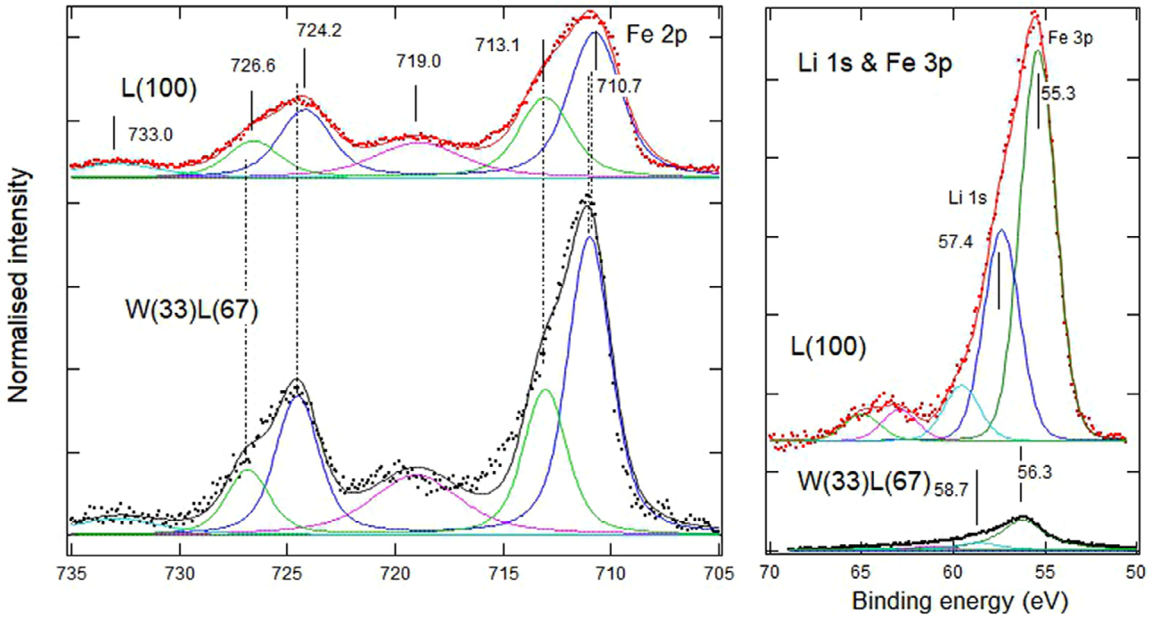

Figure 4. High resolution XPS spectra of L(100) and W(33)L(67) samples: Fe 2p (left) and Li 1s and Fe 3p (right).

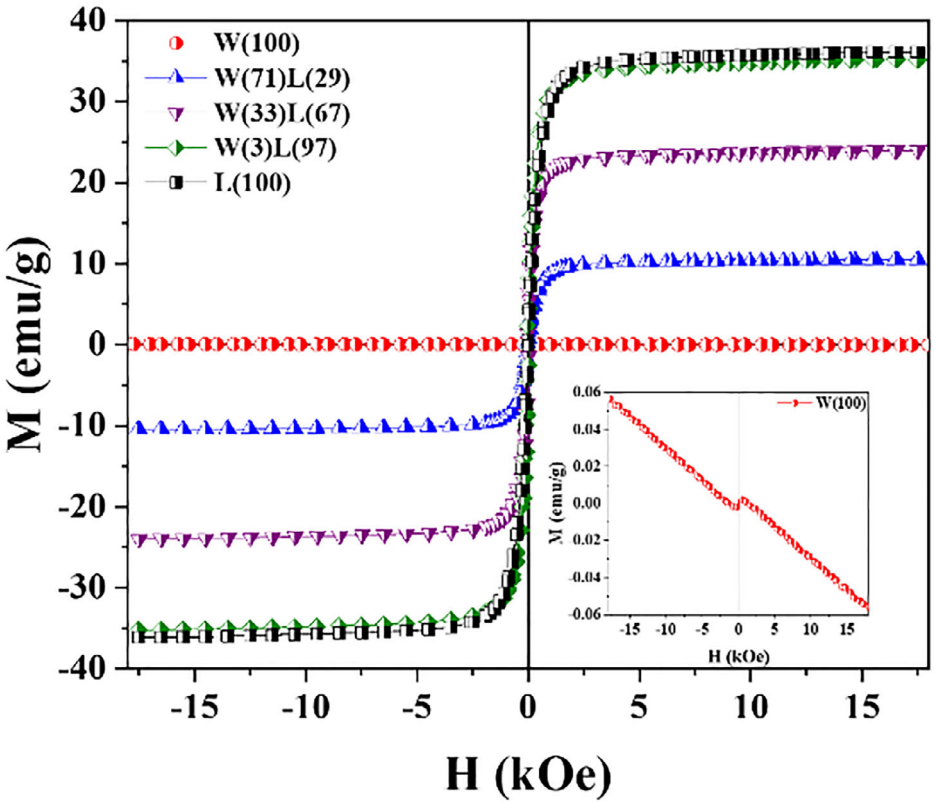

Figure 5. M-H hysteresis curves of the nanocomposites at room temperature (300 K). (Inset: Hysteresis curve of W(100) showing diamagnetic behavior).

flake-like morphology of WS_2 in the W(100) sample. The WS_2 flakes are stacked in random orientations giving rise to a floral pattern. SEM images of all the samples and the atomic percentages of different elements obtained from EDS mapping are provided in Figures S2–S6 and Tables S1–S5 (Supporting Information), respectively.

For a more accurate inspection of the internal structure and the interfaces in the nanocomposite samples, TEM analyses were performed. The observations reveal that L(100) is composed of irregularly shaped grains with sizes ranging from 200 to 700 nm (Figure 6c, white arrows), and aggregates of smaller grains (≈10 nm) (Figure 6c, dark arrows); see also Figure S7 (Supporting Information) for more details. Selected area electron diffraction (SAED) measurements allowed us to identify the large grains as the $LiFe_5O_8$ phase, while the smaller ones correspond to the $LiFeO_2$ phase (Figure S7c,d, Supporting Information). The W(100) sample is composed of thin stacked nano-platelets, which give rise to intricate nanoflakes (Figure 6d). In some cases, the nanoplatelets are oriented with their short side perpendicular to the electron beam, appearing in the image as black ribbons (dark arrows and dark square in Figure 6d), and their lateral structure and thickness can therefore be analyzed. In particular, atomic planes are visible within the thickness of the platelets and their interplanar distance, $d = 0.616(8)$ nm, obtained by the Fast Fourier Transform (FFT) of the image, corresponds to the WS_2 (002) planes (d_{WS2} (002) = 0.618 nm, hexagonal description), inset of Figure 6d; see also Figure S8 (Supporting Information) for more details. These results suggest that the larger surface area of the platelets corresponds to the (002) WS_2 planes, while the thickness of the platelets is in the c-axis direction. The thickness of the platelets varies from 1 to 70 nm, while their lateral dimensions range from 10 to 500 nm, as determined by TEM measurements. A typical TEM image of the W(33)L(67) composite is shown in Figure 6e. The irregularly shaped grains of the $LiFe_5O_8$ phase, together with the WS_2 nanoflakes, are clearly visible. The two phases are in contact with each other and uniformly distributed (see also colored EDS map in Figure S4b, Supporting Information). The presence of contacts between these phases correlates with the presence of additional minority components in the XPS spectra for the S 2p line. A very close contact between the two phases is also observed, Figure 6f, supporting the possibility of polarization effects between the dielectric and magnetic phases.

Table 1. Saturation magnetization (M_S) of the nanocomposites at 300 K. Uncertainties in the last digit are indicated in parentheses.

Sample label	M_S [emu g^{-1}]
W(100)	–
W(71)L(29)	10.5(1)
W(33)L(67)	24.0(2)
W(3)L(97)	35.2(3)
L(100)	36.1(3)

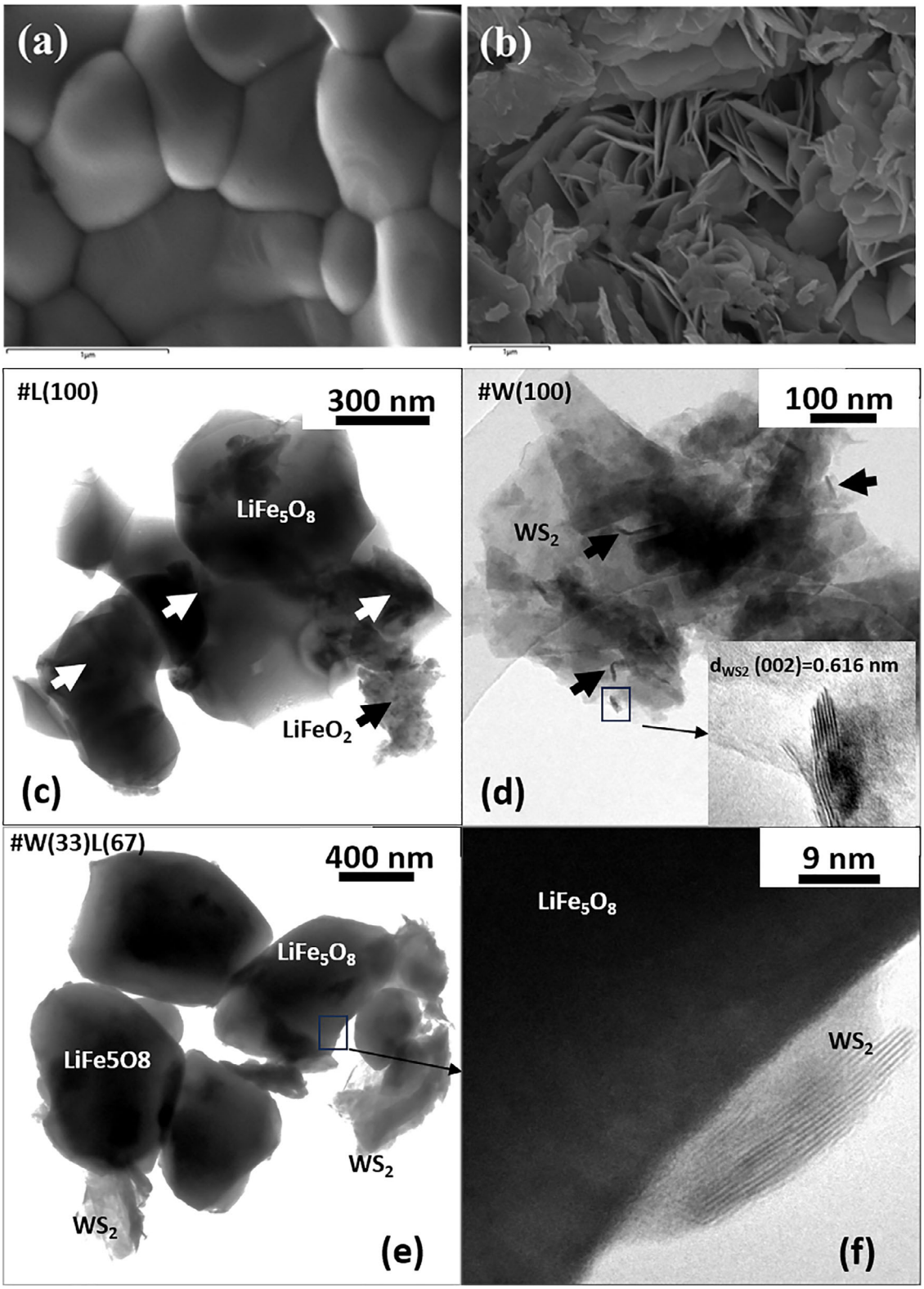

Figure 6. SEM images of: a) L(100), b) W(100); TEM images of: c) L(100) showing the typical grain structure; d) W(100) revealing that the nanoflakes are composed of thin stacked platelets (the inset shows the thickness of a platelet with visible d_{WS2}(002) lattice planes); e) W(33)L(67) where the $LiFe_5O_8$ grains are in contact with the WS_2 nanoflakes; f) a detail of the previous image showing the intimate contact between the two phases.

2.2. Tuning of EMI Shielding Properties in the Inter-Dimensional Nanocomposites

The EMI shielding performance of a sample can be analyzed based on the shielding effectiveness (*SE*) and the power fractions corresponding to reflection (*R*), absorption (*A*), and transmission (*T*). When EM waves are incident on an EMI shielding material placed inside a hollow transmission line, a part of the incident power is reflected from the air-material interface. This is denoted by the reflection coefficient (*R*), which can be used to calculate the shielding due to reflection (SE_R in dB). A fraction of the power that penetrates the material is absorbed due to dielectric and magnetic losses. The amount of absorption can be estimated from the absorption coefficient (*A*) and shielding due to absorption (SE_A in dB). The total shielding (SE_T) is then defined as the sum of the reflection and absorption shielding ($SE_R + SE_A = SE_T$). The transmission coefficient (*T*) denotes the power fraction that can transmit through the shielding material without being attenuated. The purpose of a good shielding material is to reduce *T* as much as possible. Since the law of power balance is satisfied by the condition: $R + A + T = 1$, there are two ways to reduce *T*; either by increasing reflection (*R*) of EM waves at the air-material interface or by enhancing absorption (*A*) within the material. An optimum balance between *R* and *A* may also be achieved to minimize *T* and maximize the EMI *SE*. Researchers have often used the power coefficients *R*, *A*, and *T* to quantify the reflective and absorptive capabilities of shielding materials.[13,33] Moreover, it has been discussed in literature that power coefficients represent the actual amount of reflected and absorbed power. Therefore, power coefficients are more useful in quantifying the reflection and absorption contributions to the overall shielding.[34] In a two-port transmission line method, *R*, *A*, and *T* can be calculated from the four scattering parameters (S_{11}, S_{21}, S_{12}, and S_{22}), which are measured directly by a vector network analyzer (VNA). A more detailed discussion on these parameters along with relevant mathematical expressions is provided in our previous work.[1]

Frequency-dependent shielding values (SE_R, SE_A, and SE_T in dB) of the samples are provided in **Figure 7**. From Figure 7a, it is clear that W(100) consisting of pure WS_2 has the highest shielding due to reflection (SE_R ≈16–15 dB), whereas the biphasic lithium iron oxide denoted as L(100) has a very low reflection shielding (SE_R ≈5 dB). In the nanocomposites, the SE_R values decrease with increase in ferrite content. The W(3)L(97) sample recorded the lowest SE_R value of ≈3 dB at 12.4 GHz, while its SE_R is higher than for L(100) at lower frequencies. Figure 7b depicts the frequency variation of shielding due to absorption (SE_A) for different samples. L(100) showed the lowest SE_A value (≈3 dB), while W(33)L(67) registered the maximum SE_A value of ≈48.8 dB at 12.4 GHz. This large increase in SE_A can be attributed to the magneto-dielectric synergy in the triphasic W(33)L(67) nanocomposite with nearly equal fractions of dielectric WS_2, ferrimagnetic α-$LiFe_5O_8$, and paramagnetic α-$LiFeO_2$, which increased its absorption capability.[12,35] Moreover, the formation of interfaces between α-$LiFe_5O_8$/α-$LiFeO_2$ and WS_2 also increases the interfacial polarization loss, thereby increasing the absorption of EM waves.[12,35,36]

The total shielding effectiveness (SE_T) of the samples is plotted in Figure 7c. Both W(71)L(29) and W(33)L(67) exhibit very high SE_T values (≈50–55 dB). W(100) also exhibits a very

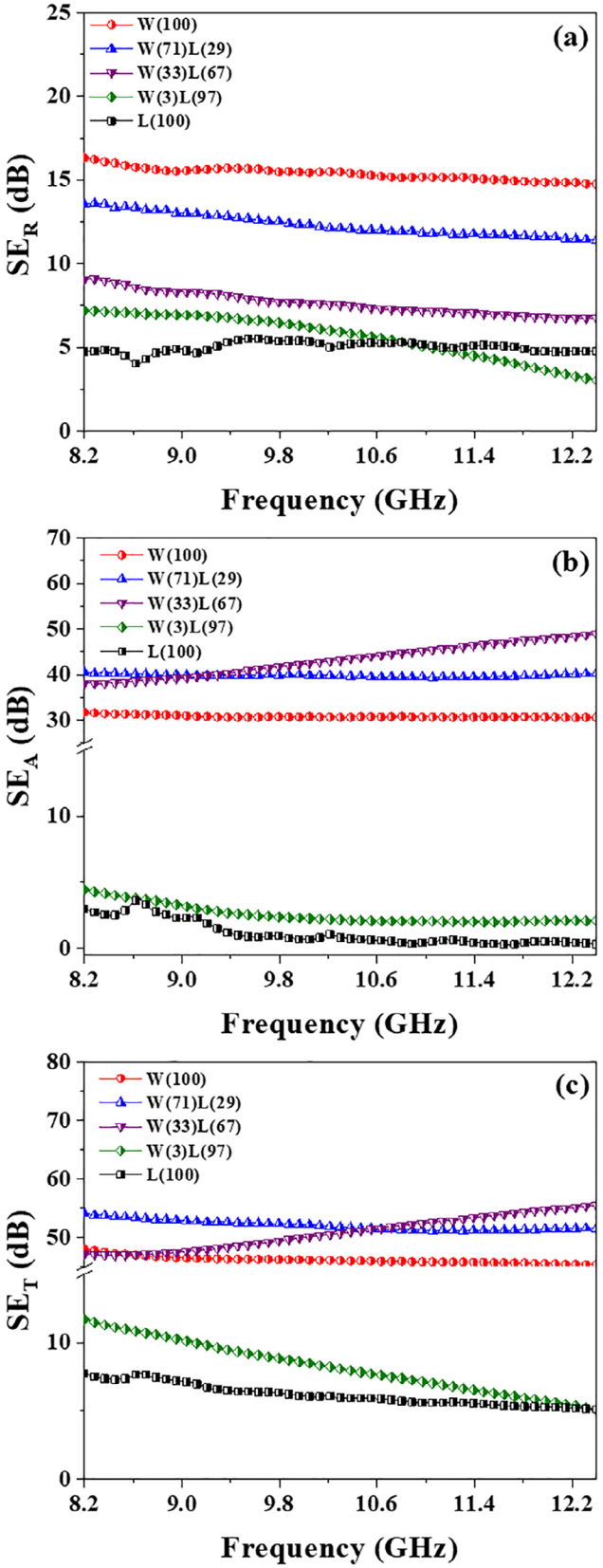

Figure 7. a) SE_R; b) SE_A; and c) SE_T as a function of frequency in the X band.

Table 2. Comparison of EMI shielding parameters (SE_R, SE_A, SE_T, SE_T/d, and A) of reported materials with this work.

Material	Frequency [GHz]	Thickness (d) [mm]	SE_R [dB]	SE_A [dB]	SE_T [dB]	SE_T/d [dB/mm]	A	Refs.
LDPE: MWCNT: GNP: $ZrFe_2O_4$ (50:5:40:5)	8.2–12.4	3.5	0.3	58.14	≈58.57	16.73	0.9	[38]
W(33)L(67)	8.2–12.4	3	6.72	48.83	55.55	18.52	0.21	This work
Mxene-$rGO_{1:2}$	8.2–12.4	3	–	–	50.7	16.9	0.3	[11]
$CoFe_2O_4$/MWCNT/GNP/LDPE (50/5/40/5)	8.2–12.4	3.5	0.36	49.55	≈50	14.29	–	[39]
16 wt% of graphene in Polypyrrole/$CoFe_2O_4$/graphene	8.2–12.4	2	≈1	≈37	≈38	19	–	[40]
LDPE: MWCNT: GNP: $LaFeO_3$ (50:5:40:5)	8.2–12.4	3.5	≈3.11	≈30.48	≈33.57	9.59	–	[41]
WS_2/rGO (5wt%)	2–18	1.5	≈7	≈28	≈32	21.33	0.2–0.4	[19]
$LiFe_5O_8$/20 wt.% Carbon black	8.2–18	3	4.85	23.17	28.02	9.34	–	[3]
$LiFe_{5-x}Dy_xO_8$/Carbon black (x = 0.1)	8.2–18	3	2.64	24.05	26.69	8.90	–	[2]
Polystyrene/MWCNT/ GNP	8.2–12.4	5.6	–	–	≈20.2	3.61	–	[42]
MoS_2-rGO/$CoFe_2O_4$	8.2–12.4	1.4	7.80	12.62	19.26	13.76	–	[12]
Polyetherimide (PEI)/graphene@Fe_3O_4	8–12	2.5	≈0.5	≈17.3	14.3–18.2	7.28	–	[14]
MoS_2-rGO/Fe_3O_4	8.2–12.4	1.3	~3.73	≈4.53	≈8.27	6.36	0.25–0.3	[13]
PLA/10C@PBS/BN (S(5:5)-10B5C)	8.2–12.4	3	–	–	41.06	13.69	0.2–0.3	[43]

impressive SE_T value of 48–45 dB. However, both W(100) and W(71)L(29) have much higher SE_R values than W(33)L(67). Therefore, W(33)L(67) is by far the better absorber among the nanocomposites for the majority of the X-band frequency range. In **Table 2**, the shielding parameters of the nanocomposites have been compared with those of other composites reported in literature. For a fair comparison, the total shielding effectiveness (SE_T) was normalized with the sample thickness (d). The quantity SE_T/d (dB mm^{-1}) was defined as total shielding effectiveness (SE_T) per unit thickness (d) as per convention found in literature.[37]

The absorption capabilities of the samples can be better understood by studying the frequency variation of R, A, and T (**Figure 8**). The reflection coefficient (R), plotted in Figure 8a, is a measure of the fraction of incident power that is reflected. If R is equal to 0.50, then 50% of the incident power is reflected. For W(100), R is ≈0.97, which implies that almost 97% of the incident power was reflected at the air-material interface. The diamagnetic behavior of WS_2 observed in the room temperature M-H curve (Figure 5, inset) may explain the high reflection observed in W(100). Diamagnetic materials repel externally applied magnetic fields, which can result in high reflection of EM waves at the air-material interface. As the wt. % of biphasic lithium iron oxide increased, the value of R decreased. For W(3)L(97), R reached a minimum value of 0.50 at 12.4 GHz. However, for a major part of the X band, L(100) exhibited the lowest value of R among all the samples. The absorption coefficient (A) plotted in Figure 8b gives an estimate of the amount of incident power that is absorbed within the material. The absorption of EM waves requires the conversion of EM energy into heat. This can be achieved by dielectric and magnetic loss mechanisms. Absorption (A) is higher in the multiphasic nanocomposites than both W(100) and L(100). From 8.2–9 GHz, L(100) has indeed A = 0.15–0.20, but this value decreases rapidly 9 GHz onward and becomes very low at higher frequencies. In contrast, W(33)L(67) maintains a high absorption (A) value of 0.12–0.21 throughout the X band. Overall, the nanocomposites W(3)L(97) and W(33)L(67) have better absorption capabilities than both the end members, W(100) and L(100). The improvement in absorption in these multiphasic nanocomposites is attributed to the formation of interfaces between the different phases.[12] The transmission coefficient of the different samples is depicted in Figure 8c. Both W(3)L(97) and L(100) have high T values ranging from roughly 0.10 to 0.30. This indicates that almost 10–30% of the incident power passes unattenuated through these materials. The other three samples including W(100), W(71)L(29), and W(33)L(67) have negligible T values (≈0).

In Figure 8d, we show the correlation between phase percentage and power fractions of the different samples. The reflection coefficient (R) increases steadily with an increase in the WS_2-WO_3 content. Reflection in W(100) (pure WS_2) is ≈42% higher than that of L(100) (pure lithium iron oxide). The absorption coefficient (A) increases at first reaching a maximum for W(33)L(67), and then decreases with further increase in the WS_2-WO_3 content. It is observed that only a small amount (≈3 wt.%) of WS_2-WO_3 is sufficient to improve the absorption coefficient of W(3)L(97) by ≈71% compared to that of L(100). When the WS_2-WO_3 content reaches ≈33 wt.% in W(33)L(67), the absorption coefficient improves by a massive ≈147% compared to L(100). This improvement in absorption is due to the interfacial polarization loss effects. For a good shielding material, the transmission coefficient (T) must be very close to 0. In all the nanocomposites, the transmission coefficient (T) is much lower compared to that of L(100). Taking into account all the parameters, W(33)L(67) emerges as the optimum material with very high total shielding (SE_T = 55.6 dB at 12.4 GHz), high absorption shielding (SE_A = 48.8 dB at 12.4 GHz), and improved absorption coefficient (A = 0.21 at 12.4 GHz).

2.2.1. Reflection Loss (RL)

Along with EMI shielding, reflection loss (RL) is an important parameter that quantifies the microwave (EM wave) absorption

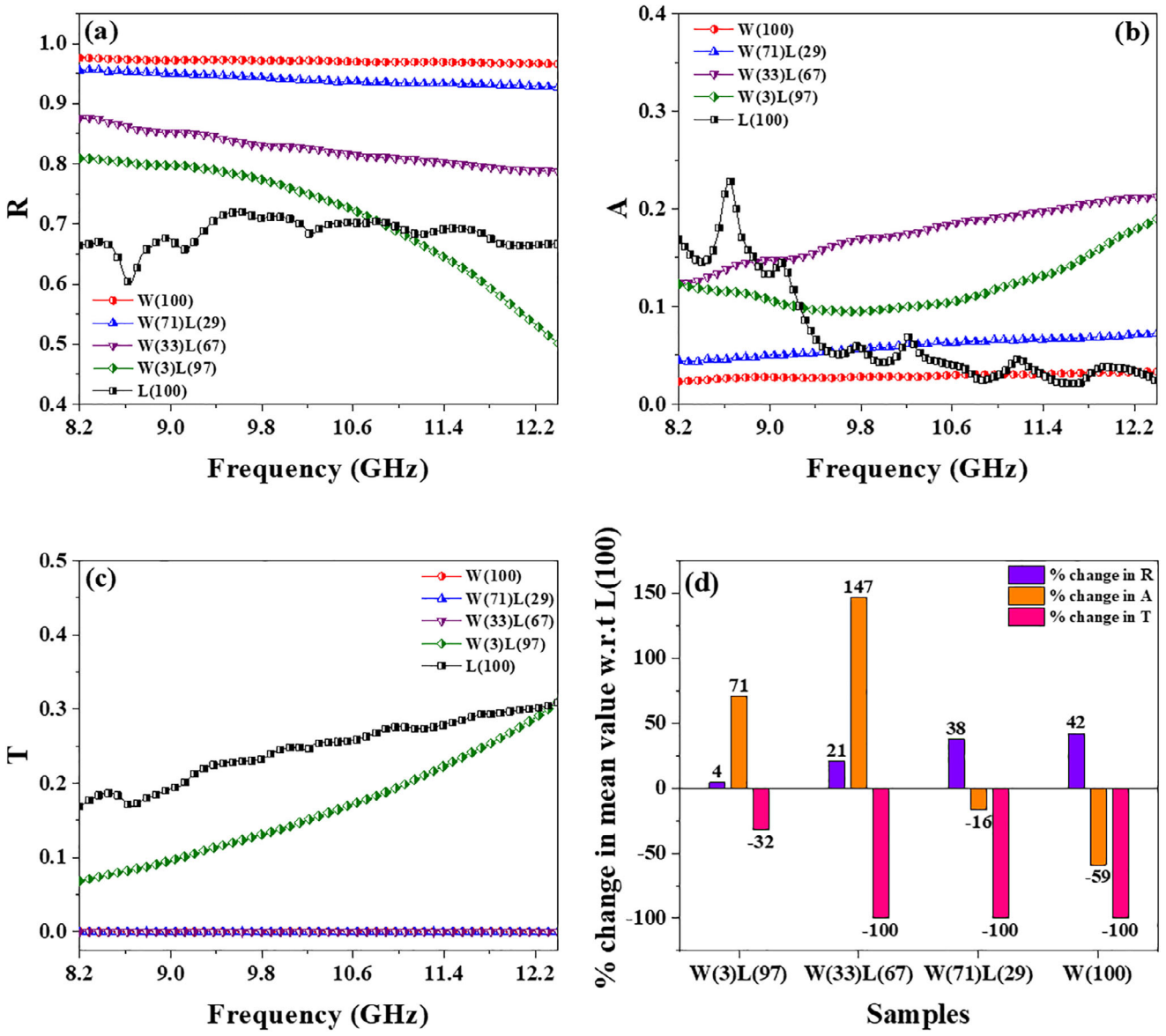

Figure 8. Frequency variation of a) *R*; b) *A*; and c) *T* in the X band; d) Percentage change in mean value of power fractions (*R*, *A*, and *T*) with respect to L(100). (Values are rounded off to the nearest integer).

capability of a material. RL (dB) quantifies the amount of absorption at the air/material interface. For a good absorber, |RL| > 10 dB is required as it corresponds to absorption of 90% of the incident electromagnetic (EM) waves. However, $|RL| > 20$ dB may be considered more suitable for applications since this corresponds to 99% absorption of EM waves. As per the transmission line theory, the reflection loss parameter can be expressed as a function of complex permittivity (ε' and ε'') and permeability (μ' and μ'').[44]

$$\mathrm{RL} = 20\log\left|\frac{Z_{\mathrm{in}} - Z_0}{Z_{\mathrm{in}} + Z_0}\right| \quad (1)$$

$$\mathrm{Z_{in}} = \mathrm{Z_0}\sqrt{\frac{\mu_{\mathrm{r}}}{\varepsilon_{\mathrm{r}}}}\tanh\left(j\frac{2\pi fd}{c}\sqrt{\mu_r\varepsilon_r}\right) \quad (2)$$

where, d is the absorber thickness, c is the speed of light in free space, f is the frequency, Z_0 is the free space impedance (≈377 Ω), and Z_{in} is the input impedance.

Figure S10a,c,e (Supporting Information) depict the RL values of the composite samples (W(71)L(29), W(33)L(67), W(3)L(97)) for multiple thicknesses. W(71)L(29) has poor reflection loss values (|RL| < 10 dB) for the majority of X-band. This is expected since the large WS_2 content results in high reflection. With a reduction in WS_2 content, the RL values improved in W(33)L(67) and W(3)L(97). W(3)L(97) showed the best RL_{min} of −70 dB at a thickness of 3.75 mm. On the other hand, W(33)L(67) exhibited RL_{min} of −55 dB at a much lower thickness of 3 mm. Moreover, for W(33)L(67), |RL| > 10 dB for all thicknesses greater than 2.25 mm. This demonstrates the superior absorption capability of the W(33)L(67) composite owing to dielectric loss and

interfacial polarization effects. High microwave absorption performance in the composite samples can be attributed to the nanoflake morphology of WS_2, which results in multiple scattering of the microwaves within the composite.[45] This dissipates the EM wave energy thereby enhancing absorption. Moreover, the formation of interfaces between WS_2 and $LiFe_5O_8$ results in interfacial polarization, which can further improve absorption.[46] The absorption of microwaves is directly related to the impedance matching at the air-material interface. Impedance matching is defined as the ratio between input impedance (Z_{in}) and free space impedance (Z_0). Absorption occurs when there is impedance matching ($Z_{in}/Z_0 = 1$) at the interface.[47] The impedance matching of the composites in X-band is depicted in Figure S10b,d,f (Supporting Information). Similar to the trend noticed in the case of RL, W(33)L(67) exhibited the best impedance matching for thicknesses of 3–3.5 mm. Impedance matching is bolstered by the presence of interfacial polarization loss.[48]

It is clearly observed from Figure S10e (Supporting Information), that the frequency of RL_{min} decreases with the increase in absorber thickness (d). This phenomenon is explained by the quarter-wavelength theory. According to this theory, for optimal microwave absorption, the absorber thickness must satisfy the criterion:[44,49]

$$d_m = \frac{n\lambda}{4} = \frac{n.c}{4f_m\sqrt{|\mu_r\varepsilon_r|}} n = 1, 3, 5, \ldots \quad (3)$$

Here, f_m, and d_m denote the frequency and thickness corresponding to RL_{min}. c is the speed of light, μ_r and ε_r are the relative permeability and permittivity, respectively. As seen in Figure S11 (Supporting Information), the experimentally obtained data points (black dots) are in good agreement with the simulated black curve. Therefore, the obtained data satisfy the quarter-wavelength model.

When electromagnetic (EM) waves travel through a material, they get attenuated. The attenuation constant (α) quantifies the spatial decay of EM waves traveling through a material. For a good absorber, the attenuation constant should be high. The attenuation constant is computed from the complex permittivity and permeability:[44]

$$\alpha = \frac{\sqrt{2}\pi f}{c}\sqrt{(\mu''\varepsilon'' - \mu'\varepsilon') + \sqrt{(\mu''\varepsilon'' - \mu'\varepsilon')^2 + (\mu'\varepsilon'' + \mu''\varepsilon')^2}} \quad (4)$$

Figure S12 (Supporting Information) depicts the attenuation constant of the composite samples as a function of frequency in the X-band. The W(33)L(67) and W(3)L(97) composites have greater attenuation constants than W(71)L(29). This indicates that both these composites are better absorbers than W(71)L(29). This aligns well with the experimentally obtained RL values (Figure S10, Supporting Information) and absorption coefficient data (Figure 8b).

2.2.2. Material Parameters

Material parameters like permittivity and permeability are usually extracted from the measured S-parameters (S_{11} and S_{21}) using the Nicolson–Ross–Weir algorithm.[1,3,50,51] However, for the nanocomposites containing WS_2, the Nicolson–Ross–Weir algorithm can be less reliable. The equations used in the algorithm tend to become algebraically unstable when $|S_{11}| \to 0$. Moreover, at very low values of $|S_{11}|$, the uncertainties in the phase measurements become large, which could lead to unreliable results.[51] The S_{11} values obtained for the samples W(100), W(71)L(29), and W(33)L(67) were small. In particular, for W(100), the S_{11} values ranged from −0.09 to −0.13. This is due to the fact that WS_2 has a very high reflection coefficient ($R \approx 0.97$) and high shielding due to reflection ($SE_R \approx 16$–15 dB). To mitigate this problem, the Reflection/Transmission Epsilon Precision mathematical model of the Keysight N1500A Materials Measurement Suite was used to calculate the complex permittivity. However, the drawback of this method is that it cannot compute the complex permeability of the sample.

The material parameters of the biphasic lithium iron oxide (L(100)) have been discussed in detail in our previous work.[1] In the current study, we focus on the material parameters of the samples containing WS_2. The complex permittivity values of the samples are plotted in **Figure 9**a,b. The polarization within a material is given by the real part of permittivity (ε″). W(33)L(67) exhibited the highest ε″ value of 12 at 8.2 GHz. The value decreased gradually at higher frequencies and reached 5.4 at 12.4 GHz. The other samples with high amount of WS_2 like W(100) and W(71)L(29) showed identical decaying trends in ε′. For W(100), ε′ varies from 9.7 to 4.3, which is in good alignment with data found in literature.[20] The decay of ε′ with increase in frequency is a common feature in many dielectrics and can be attributed to the reduction in space charge polarization effect.[52,53] According to Koop's theory,[54] the reduction in ε′ can be analyzed by assuming the dielectric material to be an inhomogeneous Maxwell-Wagner type medium composed of conducting grains separated by resistive grain boundaries. When an EM field is applied, space charge polarization builds up at the grain boundaries giving rise to the observed trend in real permittivity (ε″). Space charge effects from different species, like oxygen vacancies and grain boundary defects, may be responsible for the high value of dielectric constant (ε″) at lower frequencies. At higher frequencies, the space charge effect is reduced as the charged species are slow and lag behind the applied field.[52]

For W(3)L(97), the dielectric constant follows a slightly increasing trend. The dielectric constant increases from 8.4 at 8.2 GHz to 10 at 12.4 GHz. The small increment in the real part of permittivity may indicate the presence of a resonance peak at higher frequencies (beyond the X-band). However, in the measured frequency interval (8.2–12.4 GHz), the dielectric constant can be considered to be almost constant. It is to be noted that the dielectric response of W(3)L(97) is different than the trends observed in WS_2-rich samples, but is similar to the response observed in pure biphasic lithium iron oxide (L(100)). The dielectric constant of biphasic lithium iron oxide[1] also increases slightly from 6.3 at 8.2 GHz to 7.7 at 12.4 GHz (Figure S13, Supporting Information). The similar dielectric response between W(3)L(97) and L(100) is expected since W(3)L(97) has almost 97 wt.% of L(100). The dielectric constant of W(3)L(97) is higher than that of L(100), which is attributed to the incorporation of WS_2 in the ferrite matrix.

The imaginary part of permittivity (ε″) quantifies the ability of a material to dissipate the EM energy in the form of heat. The

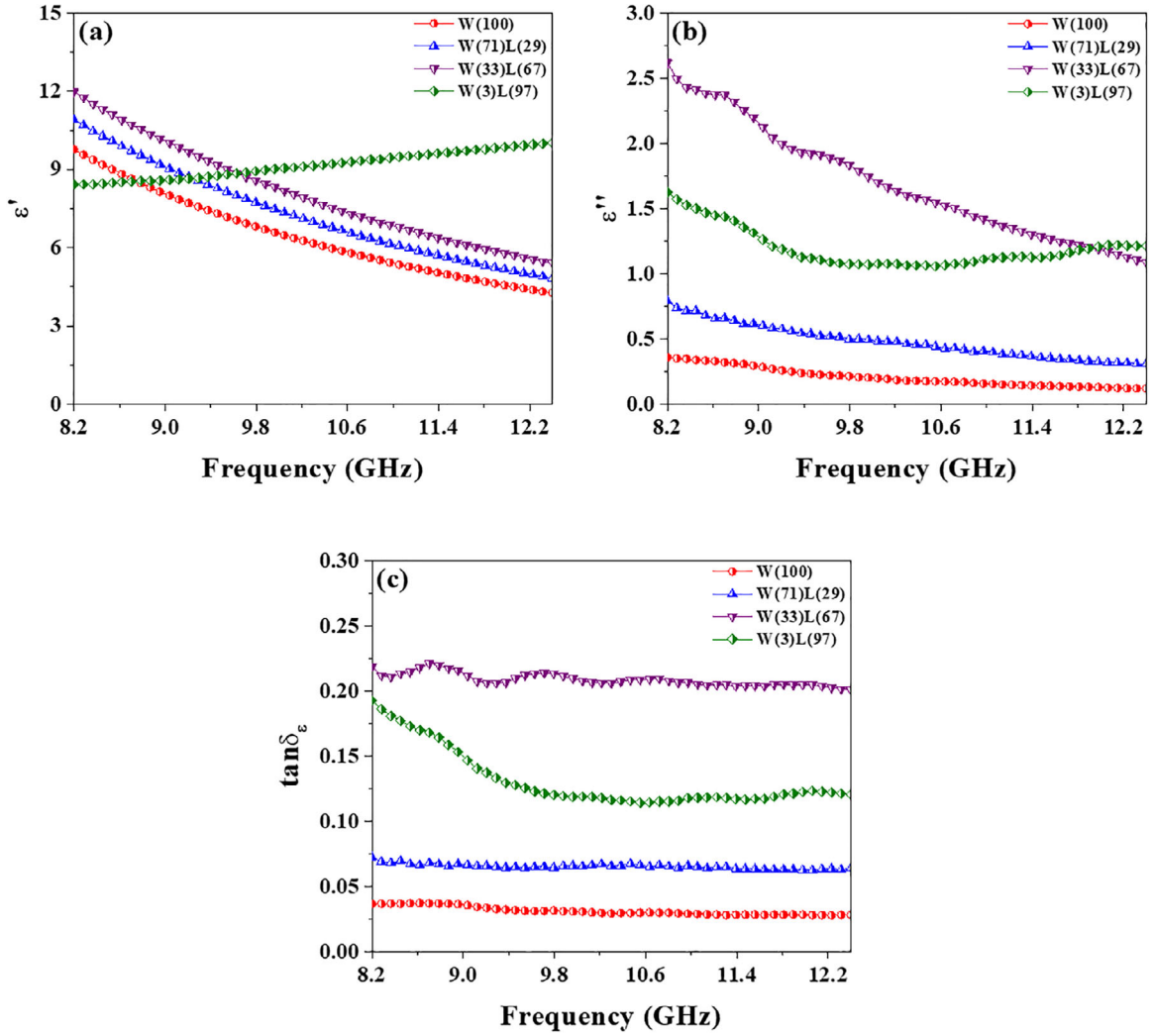

Figure 9. a) Real part of permittivity (ε′); b) Imaginary part of permittivity (ε″); c) Dielectric loss tangent ($tan\delta_\varepsilon$).

dielectric loss tangent ($tan\delta_\varepsilon = \varepsilon''/\varepsilon'$) measures the amount of dielectric loss suffered by the EM wave inside the material. In this context, it is a crucial parameter that can heavily influence the absorption capabilities of the nanocomposites. A correlation may be drawn between the variation of $tan\delta_\varepsilon$ (Figure 9c) and the absorption coefficient, *A* (Figure 8b) with respect to the phase composition of the samples. A similar trend is noticed—both $tan\delta_\varepsilon$ and *A* increase with increase in the biphasic lithium iron oxide content and attain a maximum value for the composite W(33)L(67). The end members, W(100) and L(100), have $tan\delta_\varepsilon$ values ≈0.04 and ≈0.03, respectively. Since both the end members have low loss tangents, the increase in dielectric loss tangent in the nanocomposites may be attributed mainly to the formation of interfaces between them. The interfacial effect increases gradually as more and more lithium iron oxide is incorporated and reaches an optimal point for the nanocomposite W(33)L(67). Further increase in lithium iron oxide content has a slight negative effect on $tan\delta_\varepsilon$, and this is evident for the sample W(3)L(97). This is because a majority of one phase (97% of lithium iron oxide) reduces the number of interfaces between the 0D ferrite nanoparticles and the 2D layered WS_2. To further analyze the effects of interfacial polarization, Cole–Cole plots (ε′ vs ε″) of W(100) and W(100)-based composites are depicted in Figure S14d (Supporting Information). Prominent Cole–Cole semicircles depicting relaxation mechanisms are observed for W(33)L(67) and W(3)L(97) composites. The presence of Cole–Cole semicircles confirms the presence of interfacial polarization in these composites.[46,55] The accumulation of charges at the $WS_2/LiFe_5O_8$ interface can result in significant interfacial polarization response, which attenuates EM wave energy.[46,56] On the contrary, these semicircles are not clearly visible for the W(100) and W(71)L(29) samples. This reinforces the conclusion that EMI shielding in WS_2-rich composites (W(100) and W(71)L(29)) is primarily due to reflection while the shielding mechanism is dominated by absorption in L(100)-rich composites (W(33)L(67) and W(3)L(97)). An in-depth analysis of the Cole–Cole plots is presented in Section S6 (Supporting Information).

The ac conductivity values ($\sigma_{ac} = \omega\varepsilon_o\varepsilon''$) of the samples are depicted in Figure S14c (Supporting Information). The conductivity of the samples ranges from ≈0.2 to 1.2 S m^{-1} in the X-band. The

ac conductivity follows a trend similar to dielectric loss tangent ($tan\delta_\varepsilon$) (Figure 9c). This can be explained by the fact that conduction loss is a crucial part of dielectric loss mechanisms and helps boost the absorption of EM waves.

Magnetic parameters like complex permeability (μ' and μ'') and magnetic loss tangent ($tan\delta_\mu = \mu''/\mu'$) also play an important role in the analysis of EMI shielding performance since they quantify the amount of dissipation of magnetic energy within the material. The frequency variation of magnetic parameters is depicted in Figure S14a,b (Supporting Information). Since WS_2 is a non-magnetic phase, the biphasic lithium iron oxide (L(100)) is the source of magnetic loss in all the composites. Detailed analysis of the magnetic parameters is provided in Section S6 (Supporting Information).

3. Conclusion

WS_2-WO_3/biphasic lithium iron oxide nanocomposites were prepared with different weight fractions of WS_2 and biphasic lithium iron oxide (54 wt.% α-$LiFe_5O_8$ / 46 wt.% α-$LiFeO_2$). The EMI shielding properties and dielectric parameters of the nanocomposites were studied in the X-band. The structural and morphological characterization, together with an investigation of the magnetization curves and dielectric parameters, revealed that the EMI shielding properties can be significantly altered by modifying the weight fraction of the constituent (magnetic versus dielectric) phases as well as by controlling the interfaces. The addition of WS_2 into the biphasic lithium iron oxide significantly improved the total shielding effectiveness (SE_T) of the nanocomposites. The W(33)L(67) nanocomposite achieved the highest SE_T value of ≈55.6 dB which, to the best of our knowledge, is one of the highest values reported in literature for TMDC/ferrite-based composites (Table 2). The corresponding absorption coefficient (A) was on average a massive ≈147% higher than the L(100) composite (Figure 8d). For absorption-based applications, the reflection of EM waves must be reduced to minimize secondary sources of EMI originating from the reflected waves. In such a scenario, W(33)L(67) composition is a good choice. However, high absorption also results in heating, which may be undesirable in other applications. This can be solved by using materials that have high reflection. Composites W(71)L(29) and W(100) fit nicely into this category as both have good shielding effectiveness with a significantly high amount of reflection ($R > 0.9$). The reflection coefficient (R) was on average ≈38% and ≈42% higher than L(100), respectively. Therefore, based on the application scenario, the reflection and absorption properties of WS_2/biphasic lithium iron oxide nanocomposites can be easily tuned by altering the relative phase fractions. In conclusion, this study demonstrates that the shielding performance of inter-dimensional, morphologically distinct magnetic-dielectric nanocomposites can be effectively tuned by precisely adjusting their composition, weight fraction, and interfacial characteristics.

4. Experimental Section

Preparation of WS_2 nanoflakes: Sodium tungstate dihydrate ($Na_2WO_4.2H_2O$), thiourea (CH_4N_2S), oxalic acid ($H_2C_2O_4$), and Pluronic F127 from Merck were used as precursors for hydrothermal synthesis of ultra-thin WS_2 nanoflakes. All the precursors were of analytical grade and were used without further purification. For the synthesis, sodium tungstate dihydrate (6.93 g) and thiourea (7.98 g) were weighed carefully and transferred into a beaker filled with de-ionized water (210 mL). The precursors were thoroughly dissolved by continuous magnetic stirring for 15 min after which oxalic acid (3.50 g) and Pluronic F127 (1.40 g) were added to the above solution. The solution was further stirred for 15 min. The mixture was then transferred into a 300 ml stainless-steel autoclave and heated at 240 °C for 24 h. The autoclave was allowed to naturally cool down to room temperature and the black powder product was washed several times with de-ionized water and ethanol. It was then dried in an oven at 60 °C for 12 h. Sample code W(100) was assigned to the final powder sample.

Table 3. Sample labels and corresponding composition (in wt.%) of WS_2-WO_3/lithium iron oxide nanocomposites.

Sample label	WS_2/WO_3 [wt.%]	α-$LiFe_5O_8/\alpha$-$LiFeO_2$ [wt.%]
W(100)	100	–
W(71)L(29)	71	29
W(33)L(67)	33	67
W(3)L(97)	3	97
L(100)	–	100

Preparation of Biphasic Lithium Iron Oxide: Biphasic lithium iron oxide (54 wt.% α-$LiFe_5O_8$ / 46 wt.% α-$LiFeO_2$) composite was prepared using a sol–gel auto combustion method as described in a previous work.[1] Citric acid was used as fuel and chelating agent. Analytical grade chemicals were obtained from Merck and used without further purification. In a typical synthesis, lithium nitrate and iron nitrate nonahydrate were taken in 1:2 Molar ratio and dissolved in de-ionized water. A stoichiometric amount of citric acid was added to the mixture to maintain a 1:1 Molar ratio between metal nitrates and citric acid. The mixture was then heated at 110 °C with continuous magnetic stirring. The water slowly evaporated leaving behind a reddish-brown viscous gel, which was further heated at 220 °C to obtain the powder product. The powder was crushed thoroughly in an agate mortar and annealed at 700 °C for 10 h. The final composite was assigned the sample code L(100).

Preparation of WS_2/Biphasic Lithium Iron Oxide Nanocomposites: Biphasic lithium iron oxide (L(100)) and WS_2 nanoflakes (W(100)) were weighed and dispersed in deionized water using an ultrasonic bath for 15 min. The mixture was then transferred to a stainless-steel autoclave. The autoclave was filled to 60% of its volume and placed in an oven at 130 °C for 1 h. The mixture was allowed to cool down naturally to room temperature. To facilitate precipitation, the mixture was left undisturbed overnight. The precipitate was collected and washed several times with ethanol and deionized water. The final powder was left overnight to dry at room temperature. To study the effect of phase composition on the EMI shielding properties, different weight fractions of W(100) and L(100) were used. The different compositions and the corresponding sample codes are provided in **Table 3**. Structural characterization (described later) revealed a small impurity phase of WO_3 in the nanocomposite samples. Therefore, we report the phase fractions as WS_2/WO_3 in Table 3.

Structural, Morphological, and Magnetic Characterization: X-ray diffraction was used to investigate the crystal structure and phase composition of the nanocomposites. The samples were studied under Cu-Kα radiation ($\lambda = 1.5406$ Å) using the Bragg Brentano Focusing Geometry on a Siemens D5000 X-ray diffractometer. A 2θ scan from 10° to 90° with a step size of 0.02° was used to record the diffraction patterns. Raman spectra were acquired using a Renishaw inVia Reflex confocal microscope, equipped with a frequency-doubled Nd:YAG laser operating at 532 nm with a maximum power of 43 mW at the sample surface. The spectra were collected using a 50x objective (Leica), 2400 lines mm^{-1} grating, and a laser power adjusted to 5 % of the maximum power (2.15 mW) using neutral density filters to avoid any deterioration from the laser heating. The spectra were recorded with 10 s acquisition time and 1 accumulation, covering a static scan

range of 85–1345 cm^{-1}. Prior to spectra acquisition of the samples, the spectrometer was calibrated with measurements on silicon, confirming that the characteristic Si peak was found at 520.5 cm^{-1}. X-ray photoelectron spectroscopy (XPS) was used to study the elemental composition of the samples. The XPS spectra were obtained using a PHI-5500 X-ray photoelectron spectrometer attached with an Al K-alpha source. The XPS spectra were fitted using KolXPD software.[57] Shirley background and Voigt functions were used to fit the spectra. The magnetic behavior of the samples at room temperature was investigated using a vibrating sample magnetometer (LakeShore 7404 VSM). The magnetization (*M*) versus magnetic field (*H*) hysteresis curves of all the samples were recorded in an interval of −18 to +18 kOe.

The morphology of the samples was studied using scanning electron microscopy (SEM) including elemental composition through energy-dispersive X-ray spectroscopy (EDS). A Zeiss LEO 1530 SEM equipped with an EDS detector was used for this purpose. Transmission electron microscopy (TEM) analysis was performed by a Philips CM200 electron microscope to further investigate the samples' internal morphology and specifically the interfaces between the dielectric and magnetic phases. For TEM observations, the samples in the form of powders were dispersed in ethanol and sonicated for ≈1 min. A drop of the suspension was deposited on a commercial holey-carbon grid for TEM and kept in air until complete ethanol evaporation.

EMI Shielding Measurements: Keysight N5227A Network Analyzer was used to measure the EMI shielding performance of the samples in the X-band frequency range (8.2–12.4 GHz). The network analyzer was calibrated using a two-port transmission line mode with the Keysight N9911X-WR90 mechanical calibration kit. The powder samples were pelletized in a rectangular shape (22.85 mm × 10.16 mm × 3 mm) with a hydraulic press using 30 kN force. The pellets were then placed inside a waveguide sample holder to measure the EMI shielding response. The complex permittivity (ε_r) and permeability (μ_r) values were calculated using the Keysight N1500A Materials Measurement Suite (2020).

Supporting Information

Supporting Information is available from the Wiley Online Library or from the author.

Acknowledgements

S.G., B.A., AND T.S. gratefully acknowledge funding from the Swedish Research Council (grant number 2021-03675) and Stiftelsen Olle Engkvist Byggmästare (grant number 214-0346). M.A. AND T.E. acknowledge funding from the Swedish Research Council (grant number 2023-05244) and the Swedish Energy Agency (grant number P2020-90215). J.C. gratefully acknowledges funding from ÅForsk Foundation (grant number 22-378).

Conflict of Interest

The authors declare no conflict of interest.

Data Availability Statement

The data that support the findings of this study are available from the corresponding author upon reasonable request.

Keywords

2D materials, biphasic lithium iron oxide, electromagnetic interference shielding, ferrites, interfaces, magnetic and dielectric properties, nanocomposites

Received: July 28, 2025
Revised: September 18, 2025
Published online: September 27, 2025

[1] S. Ghosh, P. Rangaiah, M. Aboulsaad, S. Slimani, J. Cedervall, B. Aslibeiki, R. Augustine, T. Edvinsson, G. Barucca, D. Peddis, T. Sarkar, *J. Alloys Compd.* **2025**, *1010*, 177017.
[2] P. P. Mohapatra, S. Ghosh, A. Jain, S. Aich, P. Dobbidi, *J. Magn. Magn. Mater.* **2023**, *573*, 170678.
[3] P. P. Mohapatra, P. Dobbidi, *Mater. Charact.* **2022**, *189*, 111985.
[4] P. Mathur, S. Raman, *J. Electron. Mater.* **2020**, *49*, 2975.
[5] G. Schmitt, J. Brachmann, b. Waldecker, l. Navarrete, t. Beyer, a. Pfeifer, w. Kubler, *Pacing Clin. Electrophysiol.* **1991**, *14*, 982.
[6] A. Balmori, *Pathophysiology* **2009**, *16*, :191.
[7] P. Raju, J. Shankar, J. Anjaiah, C. Kalyani, G. Neeraja Rani, presented at *Int. Conf. on Multifunctional Materials (ICMM-2019)*, Hyderabad, India, December **2019**.
[8] F. M. Oliveira, R. Gusmaõ, *ACS Appl. Electron. Mater.* **2020**, *2*, 0120013048.
[9] J. Liu, Z. Jia, W. Zhou, X. Liu, C. Zhang, B. Xu, G. Wu, *Chem. Eng. J.* **2022**, *429*, 132253.
[10] R. Pandey, S. Tekumalla, M. Gupta, *J. Mater. Sci.: Mater. Electron.* **2018**, *29*, 9728.
[11] Z. Fan, D. Wang, Y. Yuan, Y. Wang, Z. Cheng, Y. Liu, Z. Xie, *Chem. Eng. J.* **2020**, *381*, 122696.
[12] J. Prasad, A. K. Singh, K. K. Haldar, M. Tomar, V. Gupta, K. Singh, *RSC Adv.* *9*, **2019**, 21881.
[13] J. Prasad, A. K. Singh, J. Shah, R. K. Kotnala, K. Singh, *Mater. Res. Express* **2018**, *5*, 055028.
[14] B. Shen, W. Zhai, M. Tao, J. Ling, W. Zheng, *ACS Appl. Mater. Interfaces* **2013**, *5*, 11383.
[15] X. Duan, H. Zhang, *Chem. Rev.* **2024**, *124*, 10619.
[16] R. Kumar, N. Goel, M. Hojamberdiev, M. Kumar, *Sens. Actuators, A* **2020**, *303*, 111875.
[17] B. Wu, J. Xiao, S. Fu, H. Yin, L.u Li, J. Yao, H. Gao, *J. Colloid Interface Sci.* **2024**, *657*, 124.
[18] R. Jana, S. Ghosh, R. Bhunia, A. Chowdhury, *J. Mater. Chem. C* **2024**, *12*, 5299.
[19] D.-Q. Zhang, T.-T. Liu, J.-C. Shu, S. Liang, X.-X. Wang, J.-Y. Cheng, H. Wang, M.-S. Cao, *ACS Appl. Mater. Interfaces* **2019**, *11*, 26807.
[20] D. Zhang, T. Liu, S. Liang, J. Chai, X. Yang, J. Cheng, H. Wang, M. Cao, *Integr. Ferroelectr.* **2019**, *200*, 108.
[21] X. Zhang, H. Fei, Z. Wu, D. Wang, *Tungsten* **2019**, *1*, 101..
[22] X. H. Zhang, C. K. Yan, H. B. Cao, H. Tan, Z. Wang, *Chalcogenide Lett.* **2022**, *19*, 817.
[23] X. Zhang, W. Lei, X. Ye, C. Wang, B. Lin, H. Tang, C. Li, *Mater. Lett.* **2015**, *159*, 399.
[24] D. S. Patrick, P. Bharathi, S. Kamalakannan, J. Archana, M. Navaneethan, M. K. Mohan, *Appl. Surf. Sci.* **2024**, *642*, 158554.
[25] P. Bhatt, V. Kumar, M. Kumar Jha, N. Halder, *NanoWorld Journal* **2022**, *8*, S49.
[26] A. Berkdemir, H. R. Gutiérrez, A. R. Botello-Méndez, N. Perea-López, A. L. Elías, C.-I. Chia, B. Wang, V. H. Crespi, F. López-Urías, J.-C. Charlier, H. Terrones, M. Terrones, *Sci. Rep.* **2013**, *3*, 1755.
[27] X. Ding, T. Liu, S. Ahmed, N. Bao, J. Ding, J. Yi, *Journal of Alloys Compounds* **2019**, *772*, 740.
[28] M. F. Daniel, B. Desbat, J. C. Lassegues, B. Gerand, M. Figlarz, *J. Solid State Chem.* **1987**, *67*, 235.
[29] B. Mahler, V. Hoepfner, K. Liao, G. A. Ozin, *J. Am. Chem. Soc.* **2014**, *136*, 14121.
[30] Y. Hu, H. Zhao, M. Tan, J. Liu, X. Shu, M. Zhang, S. Liu, Q. Ran, H. Li, X. Liu, *J. Mater. Sci. Technol.* **2020**, *55*, 173.

[31] S. Subash, S. Udhayakumar, L. Kumaresan, L. N. Patro, V. Kumaran, E. S. Kumar, M. Navaneethan, D. K. Kim, K. K. Bharathi, *Electrochim. Acta* **2023**, *454*, 142318.
[32] T. Yamashita, P. Hayes, *Appl. Surf. Sci.* **2008**, *254*, 2441.
[33] Y. Fei, M. Liang, Y. Chen, H. Zou, *Ind. Eng. Chem. Res.* **2020**, *59*, 154.
[34] M. Peng, F. Qin, *J. Appl. Phys.* **2021**, *130*, 225108.
[35] M. L. Huang, C. L. Luo, C. Sun, K. Y. Zhao, Y. Ou, M. Wang, *J. Mater. Sci. Technol.* **2024**, *178*, 201.
[36] C. Sun, C. Cheng, M. Sun, Z. Zhang, *J. Magn. Magn. Mater.* **2019**, *482*, 79.
[37] T. Kuang, J. Zhang, G.-M. Huang, T. Liu, Z.-X. Huang, *Nano Energy* **2024**, *128*, 109877.
[38] M. Praveen, B. P. Harichandra, R. H. Krishna, M. Kumar, G. S. Karthikeya, H. R. Swamy, S. Koul, B. M. Nagabhushana, *Colloids Surf. A* **2024**, *699*, 134535.
[39] M. Praveen, G. S. Karthikeya, R. H. Krishna, G. M. Mamatha, C. Manjunatha, A. Khosla, B. M. Nagabhushana, *Diamond Relat. Mater.* **2022**, *130*, 109501.
[40] N. Gill, A. L. Sharma, V. Gupta, M. Tomar, O. P. Pandey, D. P. Singh, *J. Alloys Compd.* **2019**, *797*, 1190.
[41] T. M. Madhu Kumar, H. J. Kini, M. Praveen, M. Kumar, *Diamond Relat. Mater.* **2024**, *141*, 110701.
[42] S. Maiti, N. K. Shrivastava, S. Suin, B. B. Khatua, *ACS Appl. Mater. Interfaces* **2013**, *5*, 4712.
[43] H. Guo, H. Feng, T. Liu, T. Kuang, *Polymer* **2025**, *316*, 127891.
[44] M. Mahmoodi, B. Aslibeiki, S. Ghosh, L. Hasani, S. Slimani, L. Vattuone, D. Peddis, T. Sarkar, *Adv. Sustainable Syst.* **2025**, *9*, 2400549.
[45] B. Zhao, Y. Du, H. Lv, Z. Yan, H. Jian, G. Chen, Y. Wu, B. Fan, J. Zhang, L. Wu, D. W. Zhang, R. Che, *Adv. Funct. Mater.* **2023**, *33*, 2302172.
[46] B. Zhao, Y. Du, Z. Yan, L. Rao, G. Chen, M. Yuan, L. Yang, J. Zhang, R. Che, *Adv. Funct. Mater.* **2023**, *33*, 2209924.
[47] Y. Du, Z. Yan, W. You, Q. Men, G. Chen, X. Lv, Y. Wu, K. Luo, B. Zhao, J. Zhang, R. Che, *Adv. Funct. Mater.* **2023**, *33*, 2301449.
[48] R. Cui, Y. Li, X. Zhang, Z. Duan, B. Zhao, C. Wan, *Nat. Commun.* **2025**, *16*, 5804.
[49] C. Yao, Z. Wu, J. Liu, X. Guo, W. Zhang, W. Huang, H. Zhou, *J. Mater. Sci.: Mater. Electron.* **2023**, *34*, 1213.
[50] A. M. Nicolson, G. F. Ross, *IEEE Trans. Instrum. Meas.* **1970**, *19*, 377.
[51] L. F. Chen, *Microwave Electronics*, Wiley, Hoboken, NJ **2004**.
[52] L. Chauhan, A. K. Shukla, K. Sreenivas, *Ceram. Int.* **2015**, *41*, 8341.
[53] Z. Z. Lazarevic, C. Jovalekic, D. L. Sekulic, A. Milutinovic, S. Balos, M. Slankamenac, N. Z. Romcevic, *Mater. Res. Bull.* **2013**, *48*, 4368.
[54] C. G. Koops, *Phys. Rev.* **1951**, *83*, 121.
[55] B. Zhao, Z. Yan, Y. Du, L. Rao, G. Chen, Y. Wu, L. Yang, J. Zhang, L. Wu, D. W. Zhang, R. Che, *Adv. Mater.* **2023**, *35*, 2210243.
[56] B. Zhao, Z. Yan, L. Liu, Y. Zhang, L.i Guan, X. Guo, R. Li, R. Che, R. Zhang, *Adv. Funct. Mater.* **2024**, *34*, 2314008.
[57] https://www.kolibrik.net/en/solutions-products/kolxpd (acceesed: September 2025).